ARTICLE

A Comparative Study of Honeycomb-like 2D π-Conjugated Metal-Organic Frameworks Chemiresistors: Conductivity and Channels

Ming-Shui Yao,[a] Ping Wang,[a] Yi-Fan Gu,[a] Tomoyuki Koganezawa,[b] Hirotaka Ashitani,[c] Yoshiki Kubota,[c] Zao-Ming Wang,[a] Ze-Yu Fan,[a] Ken-ichi Otake,*[a] and Susumu Kitagawa*[a]

Two-dimensional (2D) π-conjugated conductive metal-organic frameworks (cMOFs, 2DπcMOF) with modulated channel sizes and broad conductivity range have been reported in the last decade. In contrast, the corresponding comparative studies on their effects on chemiresistive sensing performances, which measure the resistive response toward external chemical stimuli, have not yet been reported. In this work, we sought to explore the structure-performance relationships of honeycomb-like 2D π-conjugated cMOFs chemiresistive gas sensors with channel size less than 2 nm (the mass transport issue) and broad conductivity range from ~10^{-8} S cm^{-1} to 1 S cm^{-1} (the charge transport issue). As a result, we found that the cMOF with the lower conductivity facilitates the much more sensitive response toward charge transfer of the adsorbed gases (R=63.5% toward 100 ppm of NH$_3$ for as prepared Cu-THQ sensor, conductivity, ~10^{-8} S cm^{-1}). Interestingly, the cMOF with the medium channel size (Cu-THHP-THQ) exhibited the fastest response speed in the sensing, although it contains the H$_2$en^{2+} as neutralizing counterions in the channels. From the evaluation of the pore size distribution, it is found that the overall porosity (meso- & micro-pores) of cMOFs, rather than the pore size of the honeycomb structure, would determine their sensing speed. When comparing the performance of two different morphologies of nanorods (NRs) and nanosheets (NSs), NRs showed a slower response and extended recovery time, which can be ascribed to the slower gas diffusion in the more extended 1D channel. Altogether, our results demonstrate the first systematic studies on the effect of various structural parameters on the chemiresistive sensor performance of cMOFs.

Introduction

In contrast to proton-/ion-conductive types,[1-4] the newly emerging electrically conductive metal-organic frameworks/porous coordination polymers (cMOFs/cPCPs),[5-7] a type of microporous crystalline materials constructed by regular coordination of organic ligands and metal nodes with effective band/hopping transport pathways,[8-11] enable their direct use as active materials in electrical devices.[12-18] The sub-class porous two dimensional (2D) π-conjugated cMOFs, constructed by the stacking of 2D layers composed of trigonal/square organic ligands and square planar mononuclear metal nodes, have been extensively studied in electrical applications such as gas sensors,[19-22] batteries,[23-25] supercapacitors,[26-28] field-effect transistors,[29-31] catalysis,[32, 33] etc. Primarily, we expect that the integration of highly tailored host−guest interactions into the porous redox-active scaffold of 2D π-conjugated cMOFs enables their excellent chemiresisitve sensing performances toward various biomarkers toxic or flammable gases, which are generally difficult to detect sensitively by traditional chemiresistors at room temperature (RT).[20-22, 34-38]

In the last decade, the honeycomb-like 2D π-conjugated cMOFs based on trigonal organic ligands have been well developed by both channel size (from 1.31 nm to 2.95 nm) and electronic structures (MX$_4$, X=O, NH, S; conductivity from ~10^{-8} S cm^{-1} to 140 S cm^{-1}).[11, 19, 35, 39-44] The variable channel size and MX$_4$ units enable the modulated channel traffic effects for gas diffusion. We recently reported the first example of dual-ligand honeycomb-like cMOFs with a medium channel size of 1.76 nm and conductivity of ~10^{-8} S cm^{-1}. The corresponding chemiresistive sensing performance, which monitors the resistive response toward the external chemical stimuli, exhibited a reversible response to 1 ppm of ammonia gas with a good signal to the noise level.[35] Comparing works of sensor arrays constructed by chemically distinct cMOFs with similar channel sizes of ~2.18 nm and varied conductivity between ~10^{-3}-2 S cm^{-1} by reported results,[37, 45] we, therefore, sought to explore further the effects of channel size less than 2 nm and broad conductivity range from ~10^{-8} S cm^{-1} to 1 S cm^{-1}.

Here, we report the comparative study of cMOFs with modulated porosity and electronic structures and their effects on chemiresistive sensing performances. Accordingly, four types of Cu based honeycomb-like 2D π-conjugated cMOFs were synthesized based on three trigonal redox-active organic

a. Institute for Integrated Cell-Material Sciences, Kyoto University Institute for Advanced Study, Kyoto University, Yoshida Ushinomiya-cho, Sakyo-ku, Kyoto 606-8501, Japan. E-mail: ootake.kenichi.8a@kyoto-u.ac.jp, kitagawa@icems.kyoto-u.ac.jp
b. Japan Synchrotron Radiation Research Institute (JASRI), 1-1-1, Kouto, Sayo-cho, Sayo-gun, Hyogo 679-5198 Japan.
c. Department of Physical Science, Graduate School of Science, Osaka Prefecture University, Osaka, Japan
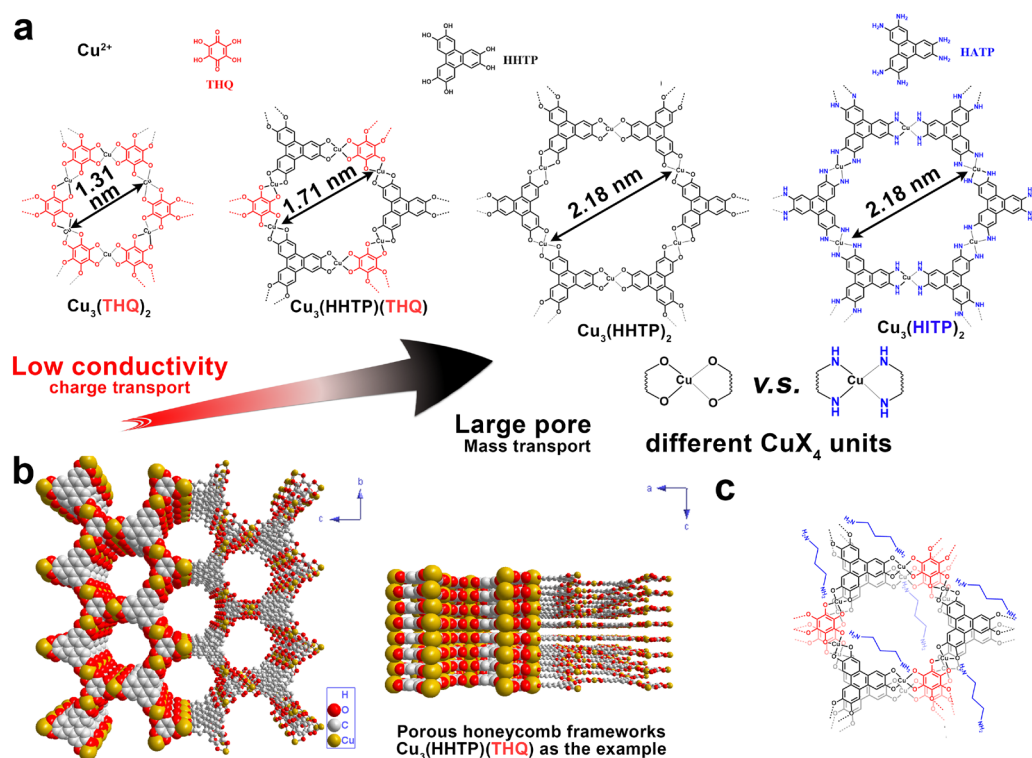
Fig. 1 Schematic illustration of (a) the structure of *c*MOFs 2D layers constructed by the coordination of Cu ions with trigonal organic ligands, (b) the porous honeycomb-like frameworks formed by the slipped-parallel stacking of 2D layers (Cu-HHTP-THQ as an example), and (c) the counterions are occupying channels of *c*MOFs with THQ ligands (Cu-HHTP-THQ as an example).

ligands (**Figure 1**a): tetrahydroxy-1,4-quinone (THQ, molecular size, ca. 0.55 nm), hexahydrotriphenylene (HHTP, molecular size, ca. 0.97 nm), and hexaaminotriphenylene (HATP, molecular size, ca. 0.97 nm). All *c*MOFs showed honeycomb-like structures with the energetically favored AB slipped-parallel stacking model where every two 2D layers are slightly slipped from each other (**Figure 1**b). Cu-HHTP and Cu-HITP are neutral frameworks without counterions in the channels after activation due to the redox-active nature of the constituent ligands. While for THQ containing *c*MOFs, because of the net negative charge (-1) of each square-planar CuO_4 center, the protonated ethylenediamine ($NH_3CH_2CH_2NH_3^{2+}$, H_2en^{2+}) as counter ions reside in the pores and significantly narrow down the practical channel size, and reduce the uncoordinated Cu sites (**Figure 1**c). In this study, the four types of *c*MOFs enable us to evaluate the structure-property relationships on chemiresistive performances; type of Cu nodes (CuO_4 or CuN_4), channel sizes, and the effect crystal morphology.

Results and discussion

All 2D π-conjugation *c*MOFs, specifically Cu-HITP, Cu-HHTP, Cu-HHTQ-THQ, and Cu-THQ, were prepared by the previously reported wet chemical methods with slight modification (Figure 1, see Experimental Section for details). For Cu-HHTP, we obtained two different morphologies, nanorods (NR) and nanosheet (NS), depending on the synthetic condition. Subsequently to the syntheses, water and methanol were used

for repeatable washing and solvent-exchanging of *c*MOFs with CuO_4 centers. For Cu-HHTP-THQ and Cu-THQ with relatively small channels, additional treatments by water for 12 h were required to ensure the removal of residual free en. In Cu-HITP with CuN_4 centers, only methanol was used for the washing (five times). Powder X-ray diffraction (PXRD) patterns of the synthesized samples were shown in **Figures 2** and S1 (Supporting Information, SI). For Cu-HHTP and Cu-HITP, the slipping between two layers is much smaller than its unit cells. Thus their unit cell parameters were described by hexagonal *P6/mmm*, with *a* = 2.18-2.23 nm, and *c* = 0.660-0.666 nm.[19] For Cu-HHTP-THQ constructed by binary ligands, unit cell parameters of activated powders were described with the smaller values of *a* = 1.71 nm and *c* = 0.627 nm with trigonal *P3m1* space group.[35] While for Cu-THQ with the most petite pore sizes among the synthesized *c*MOFs, the slipping between two layers reduces the symmetry to *C*-centered *orthorhombic* unit cell with cell parameters of *a* = 1.31 nm, *b* = 2.16 nm, and *c* = 0.59 nm.[39] With the decrease of lattice spacing along the *ab* plane due to the smaller size of ligands, the (100) peak at 2θ = ~4.8° of hexagonal Cu-HHTP or Cu-HITP shifts to the higher degree at 2θ = ~5.9° of that in trigonal Cu-HHTP-THQ, and finally reaches 2θ = ~7.9° of the (110)/(020) for *orthorhombic* Cu-THQ. As revealed by both experimental and theoretical observation,[19, 35, 39] it is well-known that the *c*MOF typically adopts the AB stacking structure wherein the 2D unit cell of one layer is slightly slipped relative to a neighboring layer. According to the calculation results on the thermodynamically favorable
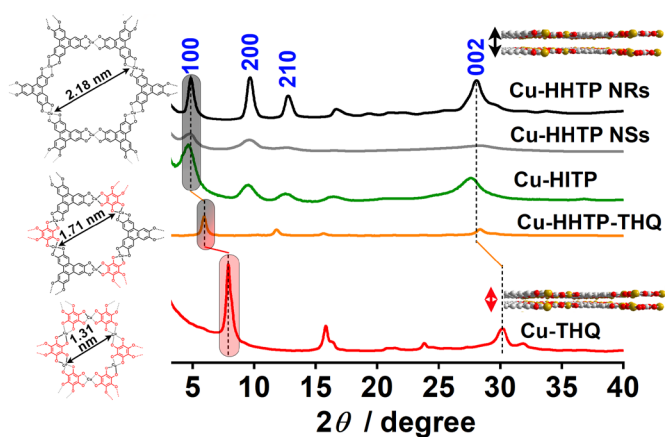
Fig. 2 PXRD patterns of Cu-HITP, Cu-HHTP NRs, Cu-HHTP NSs, Cu-HHTP-THQ, and Cu-THQ.
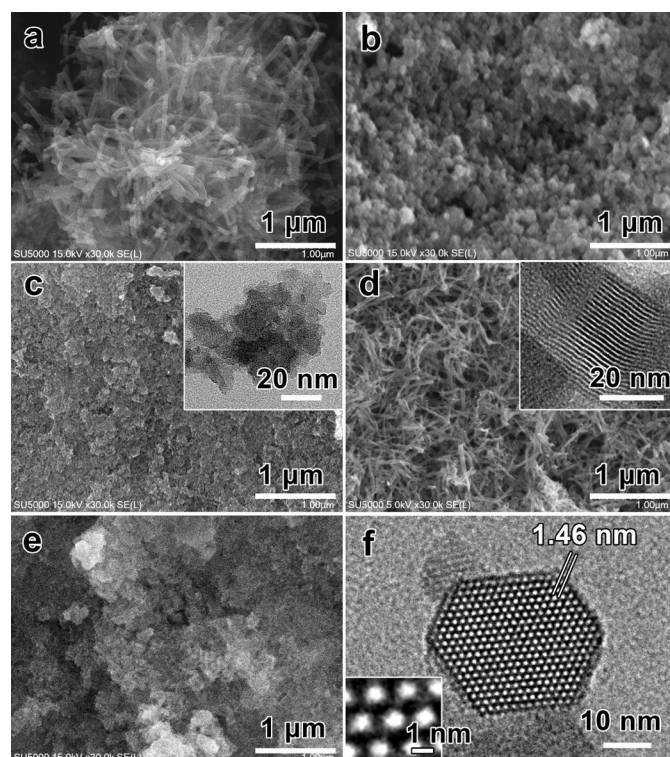

Fig. 3 SEM images of (a) Cu-HHTP NRs, (b) Cu-HHTP NSs, (c) Cu-HITP (inset, the TEM image), (d) Cu-HHTP-THQ (inset, the TEM image), and (e) Cu-THQ; (f) High-resolution TEM image of (001) face of a hexagonal Cu-HHTP-THQ NRs (the inset is the corresponding enlarged image of the center to show the visible cavity).

states,[5, 31, 35,] the slipping distance is ~0.2 nm for Cu-HHTP, Cu-HITP, and Cu-HHTP-THQ, and ~0.1 nm for Cu-THQ. The small slipping distances in Cu-THQ facilitate the effective π-π stacking of adjacent layers and thus resulting in the smaller stacking distance of <0.30 nm along the c axis, which contrasts to >0.31 nm the other three cMOFs. All the cMOFs show broad (002) peaks indicating short-range ordering along the c-axis.

Figures 3a-e show the SEM images of various cMOFs. Cu-HHTP nanorods (NRs) and Cu-HHHTP-THQ show 1D nanorod/wires with tens of nanometers and a length of hundreds of nanometers. SEM images of Cu-HHTP nanosheets (NSs), Cu-HITP, and Cu-THQ show a much smaller size of the nanosheet/plates than Cu-HHTP NRs. The high-resolution TEM

images of Cu-HHTP-THQ clearly show the typical honeycomb-like hexagonal crystal structure along the c axis, with well-defined six edges and visible cavities with the size of ~0.6-1.0 nm (Figure 3f). A lattice spacing of 1.46 nm can be well identified and indexed as (100) from both TEM images view from [001] or [010] direction (the inset of Figure 3d and Figure 3f), which is consistent with the estimated value of 1.48 nm calculated by $d(100) = \sqrt{3}/2 \times 1.71$ nm .[35] The curved channels of Cu-HHTP-THQ shown in the inset of Figure 3d are commonly observed, indicating that the dislocation of the slipping layers might be the main reason for the short-range ordering along the c-axis as characterized by the relatively broad PXRD patterns.[7]

The porous properties of cMOFs were tested by gas sorption measurements. As calculated from the N_2 sorption isotherms at 77K shown in Figure 4, similar Brunauer-Emmett-Teller (BET) surface areas of Cu-HHTP nanorods (NRs) and Cu-HITP powders were estimated. For Cu-HHTP nanosheets (NSs) with smaller particle sizes and lower crystallinity than that of NRs, a slightly lower BET value of 473.3 m^2 g^{-1} was observed. With further narrowing down the channel size, the calculated BET value of Cu-HHTP-THQ was reduced to ~430 m^2 g^{-1} due both to the smaller constituent ligand and to the existence of counterions in the channel. The significantly blocking effects of H_2en^{2+} as counter ions in the channels can also be seen from the sorption of Cu-THQ.[39] The net negative charge (-1) of each square-planar CuO_4 center suggests 1.5 H_2en^{2+} resides in a single hexagonal cavity constructed by Cu^{2+} ions and THQ ligands. Considering the occupation of H_2en^{2+} counter ions along the 1D channels, the freely accessible cavity for inert N_2 molecules in Cu-THQ is limited, which resulted in the small BET surface areas of ~136 m^2 g^{-1}.

Benefiting from their satisfied conductivity and redox-activity, all 2D cMOFs powders prepared in this work were directly used as the active material of a room temperature chemiresistive gas sensor. The thick film type gas sensors were fabricated by drop coating the methanol suspension of cMOFs on insulating substrates with pre-deposited AgPd interdigital electrodes. The gas/vapor sensing measurements were conducted using a homemade dynamic sensing setup.[35] Before measures, the sensors were activated and aged under 5V and flowing dry air at 65°C for 3 h. Then the temperature was controlled to decrease to ~25°C to reach a steady baseline. The sample integrity of cMOFs sensing films on substrates after activation and aging process were verified by the synchrotron grazing incidence wide-angle X-ray scattering (GIWAXS) measurements, which showed similar patterns with the as-prepared powders (Cu-HHTP NRs and NSs, Figure 5).

To estimate the chemiresistive sensor performance, the resistance change of the sensor under chemical stimuli was transformed to current (I) and collected by a sourcemeter under constant voltage (5 V). Figure 6a shows the dynamic sensing curve of Cu-HITP toward typical reducing gases and an oxidizing gas. Its reversible conductivity decreases toward acetone, toluene, and NH_3 indicated the behavior of p-type semiconductor, while that of NO_2 indicated n-type semiconductor behavior. The unique coexistence of n- and p-

type sensing responses suggest the coexistence of electrons and holes as charge carriers in Cu-HITP. The unrecoverable response after the exposure to 100 ppm of NO_2, though high ($R=1728.1\%$), would be due to the strong binding, resulting in the possible partial collapse of Cu-HITP frameworks upon exposure to NO_2. To overcome such a problem, the Kim group proposed introducing catalytic noble metal to realize reversible sensing because of the chemical sensitization effects of catalytic noble metal on *c*MOFs.[38]
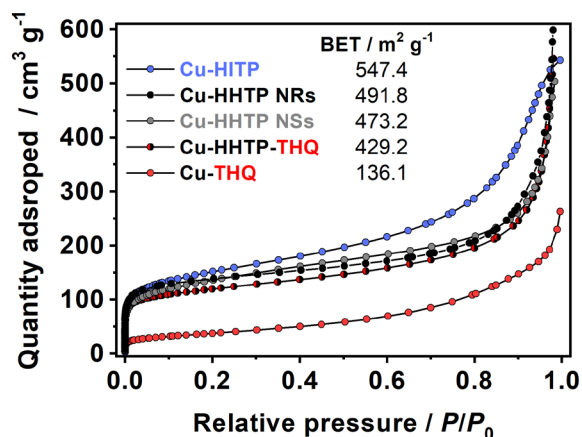

Fig. 4 N_2 sorption isotherms at 77K of Cu-HITP, Cu-HHTP NRs, Cu-HHTP NSs, Cu-HHTP-THQ, and Cu-THQ.
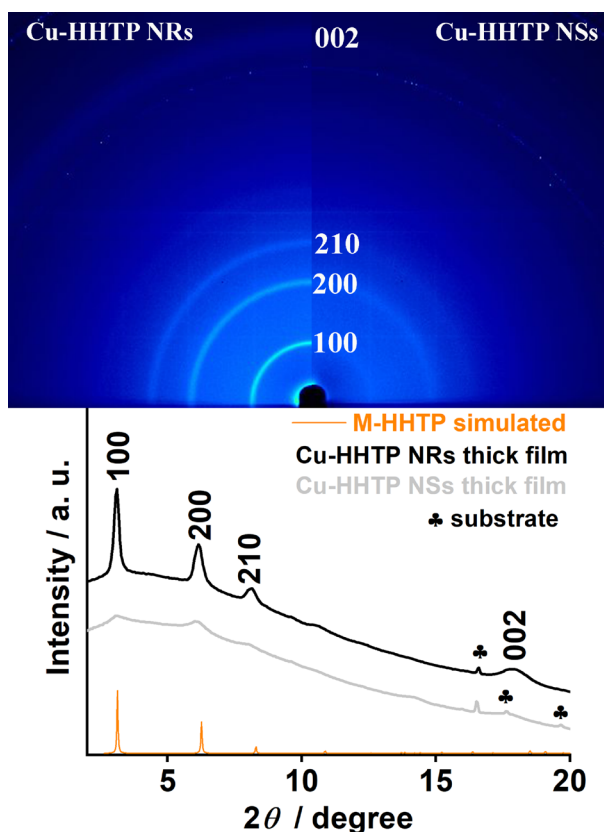

Fig. 5 The GIWAXS patterns and the converted PXRD patterns of Cu-HHTP NRs and Cu-HHTP NSs thick film on the substrate after the activation and aging process, data were collected at beamline 46XU in SPring 8, Japan (λ=1.00 Å).
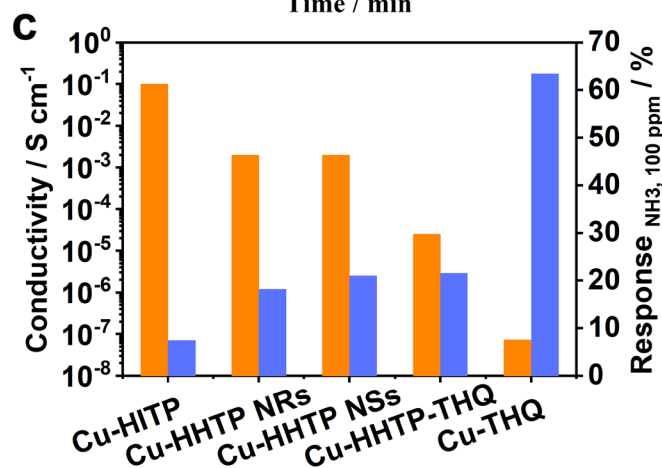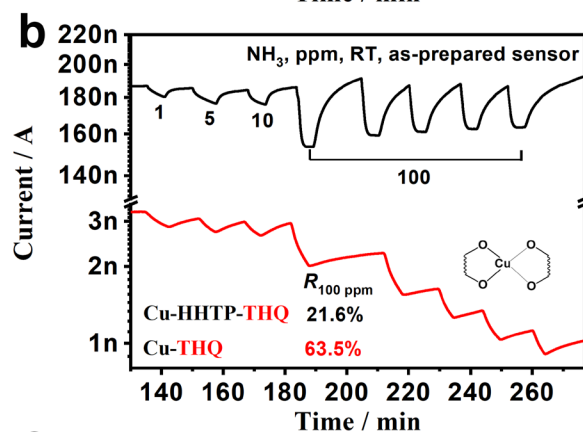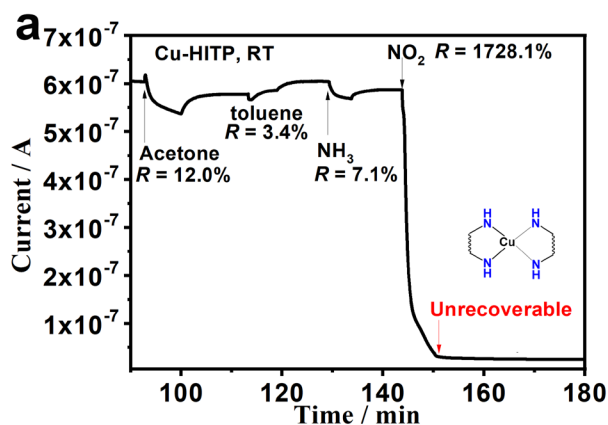

Fig. 6 (a) The dynamic sensing curve of Cu-HITP sensor toward typical reducing gases (acetone 1000 ppm, toluene 100 ppm, NH_3 100 ppm) and oxidizing gas (NO_2 100 ppm); (b) dynamic sensing curves of the Cu-HHTP-THQ and Cu-THQ sensors toward NH_3 gases with different concentration; and (c) 2-probe pellet conductivity[35, 37, 39] and response values (100 ppm of NH_3) comparison of as-prepared *c*MOF sensors.

Compared with Cu-HITP with CuN_4 center, isostructural Cu-HHTP with CuO_4 center exhibited typical p-type semiconductor behavior toward reducing gases (conductivity decrease) and oxidizing gas (conductivity increase, Figure S2, SI). The low response ($R=36.9\%$) and poor recovery instead of the unrecovered curve were observed for the Cu-HHTP NRs sensor toward 100 ppm of NO_2. In Cu-HHTP-THQ and Cu-THQ with the CuO_4 center, the use of the small THQ ligand as the component significantly reduced the conductivity by many orders of magnitude. We found that the susceptible chemiresistive

sensor with high responses could be obtained from the lower conductive *c*MOF rather than the higher conductive one (**Figure 6**b). This can be explained by the low conductivity baselines that enable the detection of low- concentration gas because of their enhanced relative resistance change caused by the small charge transfers upon the gas adsorption. This observation is also evidenced by the summarized conductivity-response comparison of the reporting *c*MOFs shown in **Figure 6**c. The response value (*R*=63.5%) of Cu-THQ sensor toward 100 ppm of NH_3 with the experimentally reached the limit of the detection value of 1 ppm (*R*=14.7%, LOD is ~0.45 ppm for *R*=10% calculated by linear log-log plots, Figure S3, SI), which is comparable with that of RT chemiresistors reported to date (Table 1).

Table 1. Room-temperature gas-sensing properties toward NH_3 of various chemiresistive gas sensors working at RT with full recovery properties. ([1] Experimental LOD, [2] IUPAC method, [3] 3RMS with simulated equation, [4] 10% response)

Material	Structure	Detection range / ppm	LOD / ppm	Ref.
Te	thick film	0.2-1	0.2	46
PEDOT [a]	thick film	10-100	10 [1]	47
Polysquaramide		10^{-5}-10^{-3}	10^{-5} [1]	48
In$_2$O$_3$	single crystal microwires	10	10 [1]	49
PbS	thick film	50	50 [1]	50
SWCNT[b]	thick film	0.02-2.8	0.02 [1] 0.003 [3]	51
SWCNT	single nanotube	1%	NA.	52
Cu-BTC@GO[c]	nanocomposites	100-500	100 [1]	53
CuTCNQ	thin film	10-99	10 [1]	54
CuTCNQF$_4$	thin film	10-99	10 [1]	55
Cu$_3$HITP$_2$	thick film	0.5-10	0.5 [1]	19
Cu$_3$(HHTP)$_2$	thin film (20 nm)	1-100	0.5 [4]	34
NiPc-Ni	thick film	2-80	0.05-0.31 [2]	20
NiPc-Cu	thick film	2-80	0.16-0.33 [2]	20
M$_3$HHTP$_2$–G[c]	thick film	5-1200	10 [2]	56
graphene	mesoporous thin film	5-100	0.16 [2]	57
graphene	thin film	NA.	1 [1]	58
black phosphorus		10-300	10 [1]	59
rGO		0.001-50	0.001 [1]	60
Ti$_3$C$_2$Tx	thin film	0.1-1	0.13 [2]	61
Modified SWCNT	thin film	1.5-20	0.1 [2]	62
Polyaniline		1-600	1 [2]	63
Cu-THQ	thick film	1-100	1 [1] ~0.45 [4]	

[a] PEDOT: poly(3,4-ethylenedioxythiophene; [b] SWCNT: single wall carbon nanotube; [c] GO: graphene oxide, G: graphene.
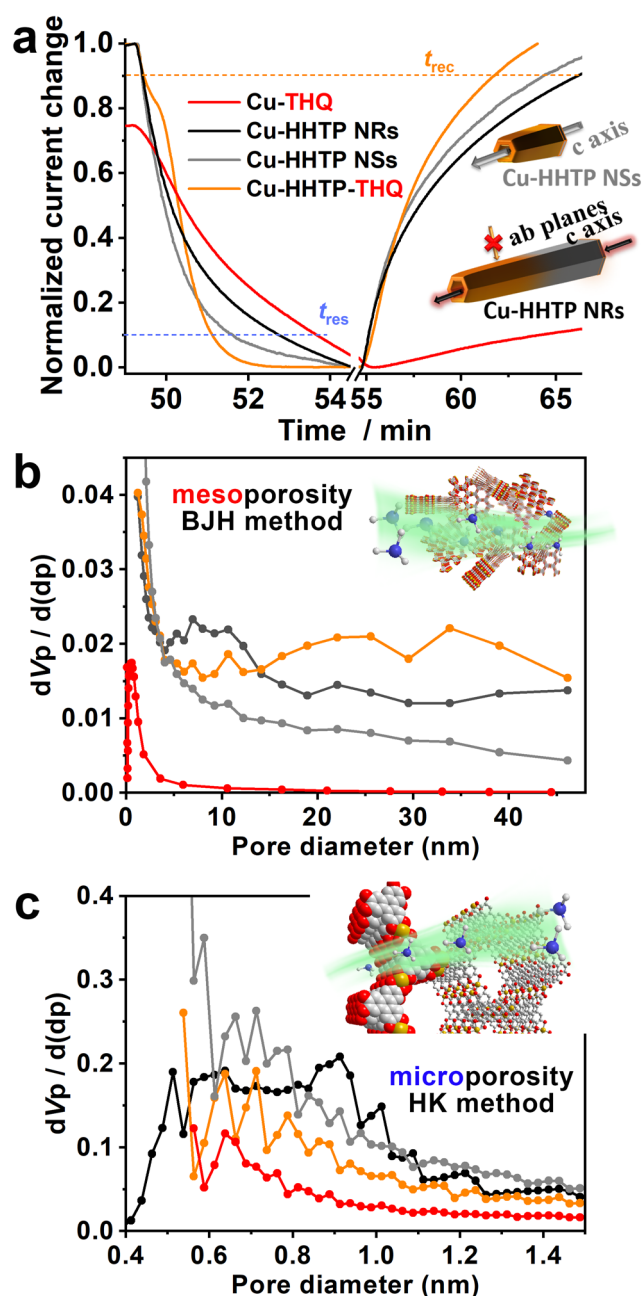

Fig. 7 (a) Normalized response-recovery curves toward 100 ppm of NH_3 gas, (b) mesoporosity distributions by BJH method (N_2, 77K), and (c) micro-porosity distributions by HK method (N_2, 77K) of different $[CuO_4]^{x-}$ units based *c*MOFs.

For the practical application of chemiresistive sensors, sensitivity and response speed are paramount. The different sizes and inner surfaces of various *c*MOFs encourage us to explore the relationship between the pore sizes and the corresponding gas diffusion behaviors in such microporous-mesoporous mixed cavities. The normalized response-recovery curves toward 100 ppm of NH_3 gas are plotted for various *c*MOFs (**Figure 7**a). As seen from the poor recovery and extended response of Cu-THQ, the poor gas diffusion of NH_3 in Cu-THQ frameworks was indicated. It is consistent with the limited freely accessible cavity and narrow pathways along the 1D channels due to the occupation of H_2en^{2+} counter ions and

the small lattice of Cu-THQ. The poor gas diffusion also led to unreliable repeatability toward five cycles of 100 ppm NH$_3$ (**Figure 6**b), indicating that its reversible working concentration range is 10 ppm and below.

In contrast, the other *c*MOFs sensors with the larger channels showed reversible chemiresistive responses. Cu-HHTP NSs with shorter lengths along the *c* axis show better response-recovery properties than Cu-HHTP NRs. Unexpectedly, Cu-HHTP-THQ with a medium channel size exhibited the fastest response speed, although it contains counter ions in channels. To figure out the origin of the observed response speed difference, pore size distribution analyses were conducted based on N$_2$ sorption curves at 77K. As shown in Figure 7b, the mesoporosity distribution calculated by Barret-Joyner-Halenda (BJH) method[64] shows the abundant mesoporosity of *c*MOFs sensors with the large channels (**Figure 7**b). At the same time, nearly non-mesoporous property of Cu-THQ was indicated. This observation of Cu-THQ may arise due to the aggregation of thin nanoplates, as seen in the SEM images. As for the micro-porosity distribution by Horvath-Kawazoe (HK) method,[65] significantly more significant amounts and broader distribution covering larger micro-pores can be seen for *c*MOFs with the larger lattices (**Figure 7**c). Combining these results, we could infer that the overall porosity (meso- & micro-pores) of *c*MOFs, rather than the pore size of the honeycomb structure, would determine their sensing speed. In the case of Cu-HHTP NRs with better multi-porosity than that of Cu-HHTP NSs, the slower response-recovery property of NRs was observed, which could be ascribed to the kinetic issue of slower gas diffusion in the more extended 1D channels along the *c* axis than that in NSs (the inset of **Figure 7**a).

Conclusions

In summary, we systematically studied the effects of channel size less than 2 nm and broad conductivity range (~10^{-8} – 0.1 S cm^{-1}) on the chemiresistive gas sensing performances of 2D π-conjugated *c*MOFs. In this study, the four types of cMOFs enable us to evaluate the structure-property relationships on chemiresistive performances; type of Cu nodes (CuO$_4$ or CuN$_4$), channel sizes, and crystal morphology. All *c*MOFs showed honeycomb-like structures with the energetically favored AB (slipped-parallel) stacking. In Cu-HITP with CuN$_4$ nodes, the unique coexistence of *n*- and *p*-type sensing responses were observed. In contrast, the other *c*MOF with CuO$_4$ nodes typically exhibited *p*-type responses. For *c*MOF with CuO$_4$ nodes, we found the chemiresistive response increases with the following trend: Cu-HHTP < Cu-HHTP-THQ < Cu-THQ. This result demonstrated that *c*MOF with the lower conductivity facilitated the higher sensitive responses toward charge transfer of the adsorbed gases (*R* = 63.5% toward 100 ppm of NH$_3$ for as prepared Cu-THQ sensor).

On the other hand, the opposite trend was found in the sensor response/recovery speed, in order by Cu-HHTP > Cu-HHTP-THQ > Cu-THQ. We discovered that multi-scale porosity (meso- & micro-) was essential to good response-recovery of *c*MOF chemiresistors. When comparing NRs and NSs of Cu-

HHTP, NRs showed a slower response and extended recovery time, which can be ascribed to the slower gas diffusion in a more extended 1D channel. Considering the excellent response of Cu-THQ even in the thick film forms, we anticipate that the gas diffusion problem can be overcome by the nanofilm fabrication (with thickness less than 100 nm,[66, 67] SURMOF[68]) or improved post-treatments to avoid unexpected aggregation of thin nanoplates. The defects design of such *c*MOFs is another way to further enhance the sensitivity due to additional active sites. The presenting comparative work would bring new understandings on the design and preparation of high-performance sensing material working at room temperature to fulfill the precise detection requirements in breath analysis, intelligent traffic, public security affairs, *etc*.

Experimental

All reagents were purchased commercially and used without further purification; the only exception is the 2,3,6,7,10,11-hexaaminotriphenylene hexahydrochloride, HATP·6HCl, was prepared according to a procedure published by D. Jiang *et al*.[69]

Preparation of Cu-HHTP NRs

As modified from our previous work,[34, 70] Cu-HHTP nanorods (NRs) were prepared by ultrasonically dissolving the mixture of copper acetate (40 mg) and HHTP (2,3,6,7,10,11-hexahydrotriphenylene, 32.5 mg) in a solution containing 14 mL of water and 14 mL of DMF. After 15 min, the resulting solution was transferred to a 50 mL sealed glass bottle and maintained at 65°C for 24 h before cooling down to room temperature. After that, the products were collected from the bottom of the reactor. The products were washed five times with fresh water and five times with methanol by ultrasonically dispersion and centrifugation at 13500 rpm for 10 min (for methanol washing, the dispersing time is 1 h for each cycle). Finally, the powders were dried under vacuum at 80°C for 12 h.

Preparation of Cu-HHTP NSs

As modified from our previous work,[34] Cu-HHTP nanosheets (NSs) were prepared by ultrasonically dispersing the mixed powders of copper acetate (40 mg) and HHTP (2,3,6,7,10,11-hexahydrotriphenylene, 32.5 mg) in 28 mL of EtOH. After 15 min, the resulting solution was transferred to a 50 mL sealed glass bottle. Subsequently, the glass bottle was maintained at 65°C for 24 h before cooling down to room temperature. After that, the products were collected and washed five times with fresh water and five times with methanol by dispersion and centrifugation at 13500 rpm for 10 min. After that, the solid materials were dried under vacuum at 80°C for 12 h.

Preparation of Cu-HITP powders

Cu-HITP powders were synthesized according to the method reported by Dincă *et al*.[19] 22.7 mg (0.028 mM) of CuSO$_4$·5H$_2$O and 0.075 mL of NH$_3$·H$_2$O were added into 2 mL DI water. Meanwhile, 10 mg (0.019 mM) of the HATP·6HCl ligand was added into 2 mL DI water. Then the two solutions were mixed

at room temperature under stirring for 3 h. Subsequently, the products were collected and washed five times with methanol. Then, the black compounds were dried under vacuum at 65°C overnight for further characterization.

Fabrication of Cu-HHTP-THQ nanowires

$Cu_3(HHTP)(THQ)$ nanowires were prepared according to our previous work.[35] By ultrasonically mixing 5 mL of aqueous solution A containing copper acetate (22 mg) and ethylenediamine (en, 11.5 μl), and 5 mL of aqueous solution B containing HHTP (2,3,6,7,10,11-hexahydrotriphenylene, 3.5 mg) and THQ (tetrahydroxy-1,4-quinone, 4.5 mg) for 15 min, the resulting solution was transferred to a 10 mL sealed test tube. Then 7.5 mL of the upper solution was removed and replaced by 3.75 mL of fresh solution A and 3.75 mL of water. Subsequently, the test tube was maintained at 65°C for 24 h before cooling down to room temperature. After that, the black products were collected from the bottom of the reactor. The products were washed five times with fresh water by dispersion and centrifugation at 3500 rpm for 10 min. Then the upper solution containing uniform $Cu_3(HHTP)(THQ)$ nanowires can be easily collected repeatedly by dispersion and centrifugation with fresh water at 2000 rpm for 3 min, followed by maintaining the obtained solution at 60°C for 12 h. The solid materials were then filtered and subsequently washed with H_2O (50 mL × 2) and acetone (25 mL × 2) and dried under vacuum at 65°C overnight for further characterization.

Preparation of Cu-THQ

Cu-THQ nanoplates were modified from our previous work[35] and the method reported by Bao *et al*.[39] By ultrasonically mixing 10 mL of solution A (water 7.5 mL, methanol 2.5 mL) containing $Cu(NO_3)_2 \cdot 3H_2O$ (53.2 mg) and en (11.5 μl) and 10 mL of aqueous solution B (water 7.5 mL, methanol 2.5 mL) containing THQ (30 mg) for 15 min, the resulting solution was transferred to a 50 mL sealed glass bottle. Then the bottle was maintained at 80°C for 14 h before cooling down to room temperature. After that, the black products were collected from the bottom of the reactor. The products were washed three times with fresh water by dispersion and centrifugation at 3500 rpm for 10 min. Then the upper solution containing Cu-THQ was collected repeatedly by dispersion and centrifugation with fresh water at 3500 rpm for 3 min, followed by maintaining the obtained solution at 60°C for 12 h. The solid materials were then filtered and subsequently washed with H_2O (50 mL × 2) and acetone (25 mL × 2) and dried under vacuum at 65°C overnight for further characterization.

Characterization

The phase and crystal structures of the products were determined by Powder X-ray diffraction (PXRD) patterns, which were recorded with beamline 02B2 at the SPring 8, Japan (λ = 0.79962 Å) and Rigaku Smartlab X-ray diffractometer with 2D array detector using Cu Kα radiation (λ = 1.54178 Å). The morphology and structure of the product were observed by scanning electron microscope (SEM, Hitachi SU5000) and transmission electron microscope (TEM, JEOL JEM-2200FS(HR)).

N_2 adsorption was measured by a BET instrument utilizing a surface area analyzer (BEL-mini X, MicrotracBEL Corp., Japan). The synchrotron GIWAXS patterns data were collected at beamline 46XU in SPring 8, Japan (λ=1.00 Å).

Gas sensor characterization

A homemade system examined the gas-sensing performance as we reported previously.[35] *c*MOFs were ultrasonically dispersed in methanol to form a suspension. Then they were drop-coated onto Al_2O_3 substrate with precoated Ag-Pd interdigital electrodes (Beijing Elite Tech Co., Ltd, China). It takes ~0.5 min to fulfill the quartz chamber when the gas flow was 600 ml min^{-1}. Low concentration (1 ppm to 10 ppm) target gas was introduced into the quartz tube by mixing the certified gas ''mixtures'' and dry air (Kyoto Teisan Co. Ltd., Japan) in a proper ratio controlled by the mass flow controllers (Horiba N100 series, Japan). The bias on the sensor was 5 V, and the current was recorded using Keithley 2602B Sourcemeter.

Conflicts of interest

There are no conflicts to declare.

Acknowledgments

Acknowledgments

References

1 S.-S. Bao, G. K. H. Shimizu and L.-M. Zheng, *Coord. Chem. Rev.*, 2019, **378**, 577-594.
2 D.-W. Lim and H. Kitagawa, *Chem. Rev.*, 2020, **120**, 8416-8467.
3 J.-S. M. Lee, K.-i. Otake and S. Kitagawa, *Coord. Chem. Rev.*, 2020, **421**, 213447.
4 S. Horike, D. Umeyama and S. Kitagawa, *Acc. Chem. Res.*, 2013, **46**, 2376-2384.
5 L. S. Xie, G. Skorupskii and M. Dinca, *Chem. Rev.*, 2020, **120**, 8536-8580.
6 S. Takaishi, M. Hosoda, T. Kajiwara, H. Miyasaka, M. Yamashita, Y. Nakanishi, Y. Kitagawa, K. Yamaguchi, A. Kobayashi and H. Kitagawa, *Inorg. Chem.*, 2009, **48**, 9048-9050.

7   J.-H. Dou, M. Q. Arguilla, Y. Luo, J. Li, W. Zhang, L. Sun, J. L. Mancuso, L. Yang, T. Chen and L. R. Parent, *Nat. Mater.*, 2021, **20**, 222-228.

8   X. Huang, P. Sheng, Z. Y. Tu, F. J. Zhang, J. H. Wang, H. Geng, Y. Zou, C. A. Di, Y. P. Yi, Y. M. Sun, W. Xu and D. B. Zhu, *Nat. Commun.*, 2015, **6**, 7408.

9   M. Hmadeh, Z. Lu, Z. Liu, F. Gándara, H. Furukawa, S. Wan, V. Augustyn, R. Chang, L. Liao, F. Zhou, E. Perre, V. Ozolins, K. Suenaga, X. Duan, B. Dunn, Y. Yamamto, O. Terasaki and O. M. Yaghi, *Chem. Mater.*, 2012, **24**, 3511-3513.

10   J. Huang, Y. He, M.-S. Yao, J. He, G. Xu, M. Zeller and Z. Xu, *J. Mater. Chem. A*, 2017, **5**, 16139-16143.

11   J. Cui and Z. Xu, *Chem. Commun.*, 2014, **50**, 3986-3988.

12   Z. Meng, R. M. Stolz, L. Mendecki and K. A. Mirica, *Chem. Rev.*, 2019, **119**, 478-598.

13   M.-S. Yao, W.-H. Li and G. Xu, *Coord. Chem. Rev.*, 2021, **426**, 213479.

14   H. Zhang, C. Gu, M.-S. Yao and S. Kitagawa, *Adv. Energy Mater.*, 2021, DOI: https://doi.org/10.1002/aenm.202100321.

15   X. Song, X. Wang, Y. Li, C. Zheng, B. Zhang, C. a. Di, F. Li, C. Jin, W. Mi and L. Chen, *Angew. Chem. Int. Ed.*, 2020, **59**, 1118-1123.

16   J. Liu, D. Yang, Y. Zhou, G. Zhang, G. Xing, Y. Liu, Y. Ma, O. Terasaki, S. Yang and L. Chen, *Angew. Chem. Int. Ed.*, 2021, **60**, 14473-14479.

17   J. Wu, J. Chen, C. Wang, Y. Zhou, K. Ba, H. Xu, W. Bao, X. Xu, A. Carlsson, S. Lazar, A. Meingast, Z. Sun and H. Deng, *Adv. Sci.*, 2020, **7**, 1903003.

18   S. Bi, H. Banda, M. Chen, L. Niu, M. Chen, T. Wu, J. Wang, R. Wang, J. Feng and T. Chen, *Nat. Mater.*, 2020, **19**, 552-558.

19   M. G. Campbell, D. Sheberla, S. F. Liu, T. M. Swager and M. Dincă, *Angew. Chem. Int. Ed.*, 2015, **127**, 4423-4426.

20   Z. Meng, A. Aykanat and K. A. Mirica, *J. Am. Chem. Soc.*, 2018, **141**, 2046-2053.

21   M. L. Aubrey, M. T. Kapelewski, J. F. Melville, J. Oktawiec, D. Presti, L. Gagliardi and J. R. Long, *J. Am. Chem. Soc.*, 2019, **141**, 5005-5013.

22   M. Wang, Z. Zhang, H. Zhong, X. Huang, W. Li, M. Hambsch, P. Zhang, Z. Wang, P. St. Petkov and T. Heine, *Angew. Chem. Int. Ed.*, 2021, DOI: https://doi.org/10.1002/anie.202104461.

23   H. Chen, Y. Xiao, C. Chen, J. Yang, C. Gao, Y. Chen, J. Wu, Y. Shen, W. Zhang and S. Li, *ACS Appl. Mater. Interfaces*, 2019, **11**, 11459-11465.

24   Y. Zang, F. Pei, J. Huang, Z. Fu, G. Xu and X. Fang, *Adv. Energy Mater.*, 2018, **8**, 1802052.

25   K. Wada, K. Sakaushi, S. Sasaki and H. Nishihara, *Angew. Chem. Int. Ed.*, 2018, **57**, 8886-8890.

26   D. Sheberla, J. C. Bachman, J. S. Elias, C. J. Sun, Y. Shao-Horn and M. Dinca, *Nat. Mater.*, 2017, **16**, 220-224.

27   D. Feng, T. Lei, M. R. Lukatskaya, J. Park, Z. Huang, M. Lee, L. Shaw, S. Chen, A. A. Yakovenko and A. Kulkarni, *Nat. Energy*, 2018, **3**, 30-36.

28   J. Liu, Y. Zhou, Z. Xie, Y. Li, Y. Liu, J. Sun, Y. Ma, O. Terasaki and L. Chen, *Angew. Chem. Int. Ed.*, 2020, **59**, 1081-1086.

29   N. Lahiri, N. Lotfizadeh, R. Tsuchikawa, V. V. Deshpande and J. Louie, *J. Am. Chem. Soc.*, 2017, **139**, 19-22.

30   G. Wu, J. Huang, Y. Zang, J. He and G. Xu, *J. Am. Chem. Soc.*, 2016, **139**, 1360-1363.

31   V. Rubio‐Giménez, M. Galbiati, J. Castells‐Gil, N. Almora‐Barrios, J. Navarro‐Sánchez, G. Escorcia‐Ariza, M. Mattera, T. Arnold, J. Rawle and S. Tatay, *Adv. Mater.*, 2018, **30**, 1704291.

32   R. Cao, J.-D. Yi, D.-H. Si, X. Xie, Q. Yin, M.-D. Zhang, Q. Wu, G.-L. Chai and Y.-B. Huang, *Angew. Chem. Int. Ed.*, 2021, DOI: https://doi.org/10.1002/anie.202104564.

33   Y. Liu, S. Li, L. Dai, J. Li, J. Lv, Z. Zhu, A. Yin, P.-F. Li and B. Wang, *Angew. Chem. Int. Ed.*, 2021, DOI: https://doi.org/10.1002/anie.202105966.

34   M.-S. Yao, X.-J. Lv, Z.-H. Fu, W.-H. Li, W.-H. Deng, G.-D. Wu and G. Xu, *Angew. Chem. Int. Ed.*, 2017, **56**, 16510-16514.

35   M. S. Yao, J. J. Zheng, A. Q. Wu, G. Xu, S. S. Nagarkar, G. Zhang, M. Tsujimoto, S. Sakaki, S. Horike, K. Otake and S. Kitagawa, *Angew. Chem. Int. Ed.*, 2020, **59**, 172-176.

36   M. S. Yao, J. W. Xiu, Q. Q. Huang, W. H. Li, W. W. Wu, A. Q. Wu, L. A. Cao, W. H. Deng, G. E. Wang and G. Xu, *Angew. Chem. Int. Ed.*, 2019, **58**, 14915-14919.

37   M. G. Campbell, S. F. Liu, T. M. Swager and M. Dinca, *J. Am. Chem. Soc.*, 2015, **137**, 13780-13783.

38   W. T. Koo, S. J. Kim, J. S. Jang, D. H. Kim and I. D. Kim, *Adv. Sci.*, 2019, **6**, 1900250.

39   J. Park, A. C. Hinckley, Z. Huang, D. Feng, A. A. Yakovenko, M. Lee, S. Chen, X. Zou and Z. Bao, *J. Am. Chem. Soc.*, 2018, **140**, 14533-14537.

40   T. Kambe, R. Sakamoto, K. Hoshiko, K. Takada, M. Miyachi, J.-H. Ryu, S. Sasaki, J. Kim, K. Nakazato, M. Takata and H. Nishihara, *J. Am. Chem. Soc.*, 2013, **135**, 2462-2465.

41   D. Sheberla, L. Sun, M. A. Blood-Forsythe, S. l. Er, C. R. Wade, C. K. Brozek, A. n. Aspuru-Guzik and M. Dincă, *J. Am. Chem. Soc.*, 2014, **136**, 8859-8862.

42   J.-H. Dou, L. Sun, Y. Ge, W. Li, C. H. Hendon, J. Li, S. Gul, J. Yano, E. A. Stach and M. Dincă, *J. Am. Chem. Soc.*, 2017, **139**, 13608-13611.

43   R. Dong, P. Han, H. Arora, M. Ballabio, M. Karakus, Z. Zhang, C. Shekhar, P. Adler, P. S. Petkov, A. Erbe, S. C. B. Mannsfeld, C. Felser, T. Heine, M. Bonn, X. Feng and E. Canovas, *Nat. Mater.*, 2018, **17**, 1027-1032.

44   A. J. Clough, J. M. Skelton, C. A. Downes, A. A. De La Rosa, J. W. Yoo, A. Walsh, B. C. Melot and S. C. Marinescu, *J. Am. Chem. Soc.*, 2017, **139**, 10863-10867.

45   M. K. Smith, K. E. Jensen, P. A. Pivak and K. A. Mirica, *Chem. Mater.*, 2016, **28**, 5264–5268.

46   L. Guan, S. Wang, W. Gu, S. Zhuang, H. Jin, W. Zhang, T. Zhang and J. Wang, *Sens. Actuators B, Chem.*, 2014, **196**, 321-327.

47   J. Jang, M. Chang and H. Yoon, *Adv. Mater.*, 2005, **17**, 1616-1620.

48   J. Zhou, H. Lin, X.-F. Cheng, J. Shu, J.-H. He, H. Li, Q.-F. Xu, N.-J. Li, D.-Y. Chen and J.-M. Lu, *Mater. Horiz.*, 2019, **6**, 554-562.

49   M. Kaur, N. Jain, K. Sharma, S. Bhattacharya, M. Roy, A. Tyagi, S. Gupta and J. Yakhmi, *Sens. Actuators B, Chem.*, 2008, **133**, 456-461.

50   H. Liu, M. Li, O. Voznyy, L. Hu, Q. Fu, D. Zhou, Z. Xia, E. H. Sargent and J. Tang, *Adv. Mater.*, 2014, **26**, 2718-2724.

51   F. Rigoni, S. Tognolini, P. Borghetti, G. Drera, S. Pagliara, A. Goldoni and L. Sangaletti, *Analyst*, 2013, **138**, 7392-7399.

52   J. Kong, N. R. Franklin, C. Zhou, M. G. Chapline, S. Peng, K. Cho and H. Dai, *Science*, 2000, **287**, 622-625.

53   N. A. Travlou, K. Singh, E. Rodríguez-Castellón and T. J. Bandosz, *J. Mater. Chem. A*, 2015, **3**, 11417-11429.

54   M. Shafiei, F. Hoshyargar, J. Lipton-Duffin, C. Piloto, N. Motta and A. P. O'Mullane, *J. Phys. Chem. C*, 2015, **119**, 22208-22216.

55   F. Hoshyargar, M. Shafiei, C. Piloto, N. Motta and A. P. O'Mullane, *J. Mater. Chem. C*, 2016, **4**, 11173-11179.

56   M. Ko, A. Aykanat, M. K. Smith and K. A. Mirica, *Sensors*, 2017, **17**, 2192.

57   R. K. Paul, S. Badhulika, N. M. Saucedo and A. Mulchandani, *Anal. Chem.*, 2012, **84**, 8171-8178.

58   F. Schedin, A. K. Geim, S. V. Morozov, E. W. Hill, P. Blake, M. I. Katsnelson and K. S. Novoselov, *Nat. Mater.*, 2007, **6**, 652.

59   M. Donarelli, L. Ottaviano, L. Giancaterini, G. Fioravanti, F. Perrozzi and C. Cantalini, *2D Materials*, 2016, **3**, 025002.

60   N. Hu, Z. Yang, Y. Wang, L. Zhang, Y. Wang, X. Huang, H. Wei, L. Wei and Y. Zhang, *Nanotechnology*, 2013, **25**, 025502.

61 S. J. Kim, H.-J. Koh, C. E. Ren, O. Kwon, K. Maleski, S.-Y. Cho, B. Anasori, C.-K. Kim, Y.-K. Choi, J. Kim, Y. Gogotsi and H.-T. Jung, *ACS Nano*, 2018, **12**, 986-993.

62 L. A. Panes-Ruiz, M. Shaygan, Y. Fu, Y. Liu, V. Khavrus, S. Oswald, T. Gemming, L. Baraban, V. Bezugly and G. Cuniberti, *ACS Sens.*, 2017, **3**, 79-86.

63 V. Chabukswar, S. Pethkar and A. A. Athawale, *Sens. Actuators B, Chem.*, 2001, **77**, 657-663.

64 E. P. Barrett, L. G. Joyner and P. P. Halenda, *J. Am. Chem. Soc.*, 1951, **73**, 373-380.

65 G. Horváth and K. Kawazoe, *J. Chem. Eng. Jpn.*, 1983, **16**, 470-475.

66 A.-Q. Wu, W.-Q. Wang, H.-B. Zhan, L.-A. Cao, X.-L. Ye, J.-J. Zheng, P. N. Kumar, K. Chiranjeevulu, W.-H. Deng, G.-E. Wang, M.-S. Yao and G. Xu, *Nano Res.*, 2021, **14**, 438-443.

67 H. Yuan, J. Cui, N. Li, M. Li, X. Yu, W. Fan, A. Karmakar, J. Dong, S. J. Pennycook, H. Cai and D. Zhao, *ACS Appl. Mater. Interfaces*, 2020, **12**, 36715-36722.

68 L. Heinke and C. Wöll, *Adv. Mater.*, 2019, **31**, 1806324.

69 L. Chen, J. Kim, T. Ishizuka, Y. Honsho, A. Saeki, S. Seki, H. Ihee and D. Jiang, *J. Am. Chem. Soc.*, 2009, **131**, 7287-7292.

70 W. H. Li, K. Ding, H. R. Tian, M. S. Yao, B. Nath, W. H. Deng, Y. Wang and G. Xu, *Adv. Funct. Mater.*, 2017, **27**, 1702067.

For Table of Contents Use Only
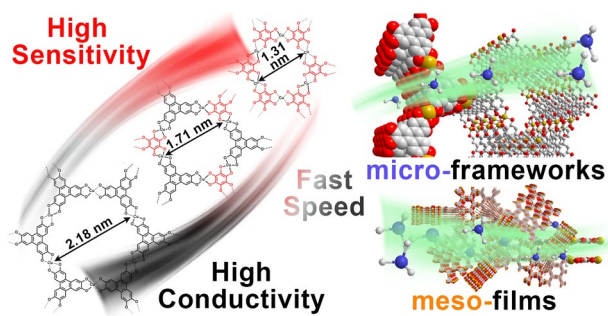
Honeycomb-like 2D π-conjugated conductive metal-organic frameworks chemiresistive gas sensors with channel size less than 2 nm (the mass transport issue) and broad conductivity range from ~10^{-8} S cm^{-1} to 1 S cm^{-1} (the charge transport issue) are studied low conductivity facilitating sensitivity, multi-scale porosity and short channel resulting fast speed.